Thermally activated intra-chain charge transport in high charge-carrier mobility copolymers

Rishat Dilmurat, Suryoday Prodhan, Linjun Wang, et al.

View Online   Export Citation   CrossMark

Thermally activated intra-chain charge transport in high charge-carrier mobility copolymers

View Online   Export Citation   CrossMark

Rishat Dilmurat,[1]   Suryoday Prodhan,[1,a)]   Linjun Wang,[2]   and David Beljonne[1,b)]

AFFILIATIONS

[1] Laboratory for Chemistry of Novel Materials, University of Mons, Place du Parc, 20, 7000 Mons, Belgium
[2] Key Laboratory of Excited-State Materials of Zhejiang Province, Department of Chemistry, Zhejiang University, Hangzhou 310027, China

[a)]**Present address:** Department of Chemistry, University of Liverpool, Liverpool L69 7ZD, United Kingdom.
Email: suryodayp@gmail.com
[b)]**Author to whom correspondence should be addressed:** David.BELJONNE@umons.ac.be

ABSTRACT

Disordered or even seemingly amorphous, donor–acceptor type, conjugated copolymers with high charge-carrier mobility have emerged as a new class of functional materials, where transport along the conjugated backbone is key. Here, we report on non-adiabatic molecular dynamics simulations of charge-carrier transport along chains of poly (indacenodithiophene-co-benzothiadiazole), within a model Hamiltonian parameterized against first-principles calculations. We predict thermally activated charge transport associated with a slightly twisted ground-state conformation, on par with experimental results. Our results also demonstrate that the energy mismatch between the hole on the donor vs the acceptor units of the copolymer drives localization of the charge carriers and limits the intra-chain charge-carrier mobility. We predict that room-temperature mobility values in excess of $10 \ \mathrm{cm^2 \ V^{-1} \ s^{-1}}$ can be achieved through proper chemical tuning of the component monomer units.

Published under an exclusive license by AIP Publishing. https://doi.org/10.1063/5.0082569

I. INTRODUCTION

Conjugated polymers are attractive materials for low-cost, large-area thin film devices, including thin-film transistors, light-emitting diodes, and photovoltaic cells, due to their solution processability, ease of functionalization, and flexibility.[1–3] Charge-carrier mobility (μ) is a ubiquitous metric for electrical transport in organic electronics, with a large number of materials being scrutinized during the last few decades.[4–11] In inorganic semiconductors, the long-range crystallinity gives rise to delocalized electronic bands and the much smaller electron–phonon coupling accounts for the scattering of the delocalized carriers with the charge-carrier mobility exhibiting inverse power-law dependence with temperature (T).[12] However, the picture is far more complex in organic semiconductors (OSCs) since all the relevant parameters, namely, electronic coupling (transfer integrals), vibrational energy, local electron–phonon coupling (reorganization energy), non-local electron–phonon coupling (dynamic disorder), and thermal energy, are of the same order of magnitude.[13] As a result, a perturbative description (either

of the electronic interaction in the hopping model or of the electron–vibrational interaction in the band model) is not valid. Consequently, a large ensemble of theoretical studies has been carried out to understand the underlying charge transport mechanism in OSCs.[14–23]

Recent experimental studies[8,24–28] of high-mobility conjugated polymers, with charge-carrier mobility approaching that of amorphous silicon (0.5–1 cm²/V s),[2] have led to the conclusion that long-range ordering of the polymer chains is not essential for high charge-carrier mobility, and the presence of short-range crystalline domains along with long "tie-chains" connecting the domains is sufficient to achieve high mobility. The large anisotropy in the intra-chain (through-bond along the polymer backbone) and inter-chain (through-space) electronic couplings signifies that the charge transport in these systems is primarily intra-molecular. As a result, it is particularly sensitive to the conformational softness of the polymer backbone. Consequently, high-rigidity polymer backbones with fused aromatic rings exhibit larger values of charge-carrier mobility.[10,29] On the other hand, the charge carriers can hop between

different polymer chains, and the wide configurational space usually leads to broad density of states with tail states at the band edge acting as an additional bottleneck for charge transport in these polymer aggregates.[30–32] In a recent work, the intra-chain charge-carrier mobility in homopolymers has been studied within a non-adiabatic molecular dynamics formalism, which demonstrates that higher stiffness of the polymer backbone is the recipe to observe large room-temperature (RT) mobility.[33] In recent experiments, Grozema and co-workers also demonstrated that intra-chain charge-carrier mobility over small length scales can be comparable to that of inorganic semiconductors,[34] while Cook et al. reported a very high charge-carrier mobility (~86 cm²/V s) along polyfluorene backbones employing the pulse radiolysis technique.[35] Improved ordering of the polymer chains in long persistence length nanofibers has also been shown to lead to enhanced exciton diffusion coefficients.[36]

Here, we address the effects of on-site energy mismatch and torsional motion along the polymer backbone on the intra-chain charge-carrier mobility in donor–acceptor copolymers, considering indacenodithiophene-co-benzothiadiazole (IDTBT) as the reference polymer. In our previous study on homopolymers,[33] we have explored the effects of torsional potential landscapes on the intra-chain charge-carrier mobility and demonstrated that RT mobility can be enhanced by an order of magnitude for planar, stiffer polymer chains. In a separate study, Manurung and co-workers recently demonstrated that the position of the highest occupied molecular orbitals (HOMOs) of the constituent monomers of a p-type copolymer can have significant effect on the localization length of the charge carrier and in effect on the mobility.[32] On account of the similar magnitude of the intra-chain electronic couplings to the (local and/or non-local) electron–phonon couplings, we consider electronic and nuclear motion simultaneously and resort to mixed quantum–classical dynamics simulations based on a Holstein–Peierls type model Hamiltonian. While a full quantum dynamics study of the nuclear motion is computationally prohibitive to explore large chemical and parameter space and is limited to small size systems,[37,38] mixed quantum–classical dynamics approaches have been adopted successfully in the study of molecular crystals[21,23,39,40] and polymers.[33,41] Since the temperature dependence of μ primarily stems from low-frequency vibrations ($\leq$100 cm⁻¹) and we are mostly interested in the room temperature properties, nuclear quantum effects such as tunneling can be neglected[42,43] and a classical description of the nuclear motion is a reasonable approximation. Nonetheless, the present study considers the feedback effect of the nuclear motion (polaronic effect) explicitly and goes beyond the conventional incoherent hopping description of charge transport in amorphous materials.[20,44,45]

This paper is organized as follows: In Sec. II, we introduce the model Hamiltonian and give a detailed description of the non-adiabatic molecular dynamics technique employed in this study. In Sec. III, we detail the calculations of the relevant parameters and analyze the results. In Sec. IV, we summarize and conclude our study.

II. MODEL HAMILTONIAN AND METHODOLOGY

In the present study, the donor–acceptor type conjugated copolymer chain is coarse-grained as a one-dimensional array of N monomers (. . .DADADA. . .) with the open boundary condition, where each monomer (donor or acceptor moiety) k is associated with a single frontier molecular orbital $|k\rangle$. We consider the highest occupied molecular orbitals (HOMOs) of the donor and acceptor moieties since we are primarily interested in p-type transport. The linear chain is described within a Su–Schrieffer–Heeger (SSH)-type model Hamiltonian, which considers both local and non-local electron–phonon couplings.[46] The total Hamiltonian of the chain can be generally expressed as

$$H = H_e + H_n. \tag{1}$$

The electronic part of the Hamiltonian (H_e) is represented by

$$H_e = \sum_{k=1}^{N} (\varepsilon_k + \alpha_k x_k)|k\rangle\langle k| + \sum_{k=2}^{N} \beta|\cos(\theta_{k,k-1})|[|k\rangle\langle k-1| + |k-1\rangle\langle k|], \tag{2}$$

while the nuclear part of the Hamiltonian (H_n) is represented by

$$H_n = \sum_{k=1}^{N} \frac{1}{2}\left[m_k v_k^2 + I_k \omega_k^2 + K_x x_k^2\right] + \sum_{k=2}^{N} \frac{K_\theta}{2}(\theta_{k,k-1} - \theta_{eq})^2. \tag{3}$$

ε_k is the on-site energy of the donor/acceptor moiety in the neutral ground-state equilibrium geometry (the corresponding energy mismatch is one of the factors explored here). Dynamics of the ions is described by two effective, classical, harmonic vibrational degrees of freedom x_k and $\theta_{k,k'}$. The intra-monomer mode (x_k) accounts for the change in monomer geometry on the addition of an excess charge; the kth monomer energy gets linearly modulated with x_k by the local electron–phonon coupling constant α_k. On the other hand, $\theta_{k,k'}$ represents the torsion between successive monomer units k and k' along the polymer axis and sinusoidally modulates the nearest-neighbor electronic coupling (non-local electron–phonon coupling). Numerically, $\theta_{k,k'}$ is decoupled by considering the orientation of individual monomer θ_k with respect to a fixed monomer at the boundary ($\theta_1 = 0$) and the time evolution of $\theta_{k,k'}$ is described by the simultaneous time evolution of θ_k and $\theta_{k'}$, since $\theta_{k,k'} = \theta_k - \theta_{k'}$. θ_{eq} is the equilibrium value of the inter-monomer torsion angle in the charge-neutral polymer chain, while β is the maximum electronic coupling achieved when $\theta_{k,k-1} = 0°$ or $180°$. m_k (I_k) corresponds to the effective mass (moment of inertia) of monomer k, while $v_k(\omega_k)$ corresponds to the linear (angular) velocity; K_x and K_θ are the intra-monomer vibrational force constant and inter-monomer torsional stiffness constant, respectively.

To probe the charge-carrier dynamics efficiently, we resort to a state-of-the-art non-adiabatic molecular dynamics technique, namely, the crossing-classified and corrected variant of subspace surface hopping algorithm.[47,48] This is a variant of Tully's fewest switches surface hopping (FSSH) algorithm[49] with better detailed balance and utilizes an ensemble of independent trajectories to represent the dynamics.[50] The system occupies an "active" potential energy surface (PES) at each time step along an individual trajectory, and in contrast to the Ehrenfest mean field dynamics, stochastic "hops" between different PESs are included to maintain the internal consistency, i.e., the fraction of trajectories on each PES should agree to the corresponding quantum population obtained by solving the time-dependent Schrödinger equation (TDSE).[50] If the charge-carrier wavepacket $\Psi(t)$ is represented in

the adiabatic basis of the electronic Hamiltonian ($\{|\psi_i\rangle\}$), $\Psi(t)$ = $\sum_i w_i(t)\psi_i(\{x_k(t)\}, \{\theta_{k,k-1}(t)\})$, the TDSE is given by

$$\dot{w}_i(t) = \left[\frac{w_i(t)E_i(\{x_k(t)\}, \{\theta_k(t)\})}{i\hbar} \right] - \sum_{j\neq i} w_j(t)\left[\sum_k \left(v_k \cdot d_{ij}^{k,x} + \omega_k \cdot d_{ij}^{k,\theta} \right) \right], \quad (4)$$

where $d_{ij}^{k,x(\theta)} = \langle \psi_i(\{x_k(t)\}, \{\theta_k(t)\}) | \partial\psi_j(\{x_k(t)\}, \{\theta_k(t)\})/\partial x(\theta)_k \rangle$ are the non-adiabatic couplings.

Before the dynamics simulation, the initial system is optimized and relaxed to the bottom of the energy band (see the supplementary material of Ref. 33 for a detailed procedure). The optimized geometry $\left(\{x_{k;opt}\}, \{\theta_{k;opt}\}\right)$ is stored and employed to set the initial values of $\{x_k\}$ and $\{\theta_k\}$ for each surface hopping trajectory. In addition, the optimized wavefunction $|\Psi_{opt}\rangle$ is also stored to set the initial wavefunction for each surface hopping trajectory. The steps of the algorithm along an individual trajectory are as follows:

1. The initial values of x_k and θ_k are determined from the Gaussian distributions about $x_{k;opt}$ and $\theta_{k;opt}$ with variance $k_B T/K_x$ and $k_B T/2K_\theta$, respectively. The initial values of the velocities v_k and ω_k are obtained from the Gaussian distributions with variance $k_B T/m_k$ and $k_B T/I_k$ (k_B being the Boltzmann constant). Employing the initial coordinates ($\{x_k\}, \{\theta_k\}$), the adiabatic states at $t = 0$ ($\{|\psi_k(0)\rangle\}$) are obtained through diagonalizing the electronic Hamiltonian. Then, we calculate the absolute overlap of each adiabatic state with the geometry-optimized wavefunction $S_k = \langle \Psi_{opt}|\psi_k(0)\rangle$. The adiabatic state with the highest overlap $|\psi_a(0)\rangle$ is chosen as the active PES at time $t = 0$, and the initial wavefunction of the electronic system is set by collapsing $|\Psi_{opt}\rangle$ to $|\psi_a(0)\rangle$.

2. Non-adiabatic coupling vectors at time t between the active state and all other adiabatic states are calculated using the Hellmann–Feynman theorem.[21,33]

3. The nuclear dynamics for the vibrational modes x_k and θ_k are described by the Langevin equations,

$$m_k\ddot{x}_k = -\frac{\partial\langle\psi_a|H|\psi_a\rangle}{\partial x_k} - \gamma m_k v_k + \xi_x, \quad (5)$$

$$I_k\ddot{\theta}_k = -\frac{\partial\langle\psi_a|H|\psi_a\rangle}{\partial\theta_k} - \gamma I_k \omega_k + \xi_\theta, \quad (6)$$

where "a" designates the active PES, γ is the friction coefficient characterizing system–bath interactions, and $\xi_{x(\theta)}$ is the Markovian Gaussian random force with standard deviation $\sqrt{2\gamma m_k k_B T/dt}$ $\left(\sqrt{2\gamma I_k k_B T/dt}\right)$, with dt being the time step size. The standard fourth order Runge–Kutta algorithm is employed to solve Eqs. (5) and (6).[21]

4. The wavepacket propagation is carried out in the locally diabatic basis, proposed by Granucci and co-workers,[51,52] which does not involve the non-adiabatic couplings explicitly and shows fast time step size convergence.[43,53] In this algorithm, the adiabatic states at time t correspond to the basis for

representing the wavefunction at any time τ within the time interval $[t, t + dt]$,

$$\Psi(\tau) = \sum_i w_i^{LD}(\tau)\psi_i(\{x_k(t)\}, \{\theta_k(t)\}). \quad (7)$$

Since the electronic Hamiltonian is diagonal in the adiabatic basis, the time-evolved coefficients are simply given by

$$w_i^{LD}(\tau) = w_i(t)\exp\left(\frac{E_i(t)(\tau - t)}{i\hbar}\right). \quad (8)$$

However, the adiabatic representation is more suitable for the calculation of the non-adiabatic coupling terms; therefore, the wavefunction is converted back to the adiabatic representation by $w_i(\tau) = \sum_j w_j^{LD} U_{ji}^*$, where

$$U_{ji} = \langle \psi_j(\{x_k(t)\}, \{\theta_k(t)\}) | \psi_i(\{x_k(\tau)\}, \{\theta_k(\tau)\})\rangle. \quad (9)$$

In our algorithm, we consider the adiabatic states at time t as the locally diabatic basis to propagate the electronic wavefunction during the time interval $[t, t + dt]$ with Eq. (8). Representation transformation is then utilized to obtain the expansion coefficients in the adiabatic basis at time $t + dt$. Similarly, the adiabatic states at time $t + dt$ are also employed as the locally diabatic basis for the next iteration.

5. A subset of adiabatic states is constructed, which constitute the subspace for surface hopping.[48] The subspace at time t is constructed by choosing M states with highest quantum populations at time t ($P_i(t) = |w_i(t)|^2$), and the current active state "a" is manually included if not picked up before. Afterward, we calculate the absolute overlap of every adiabatic state j at time $t + dt$ with these M selected states, $S_j = \sum_{k=1}^M |\langle\psi_k(t)|\psi_j(t+dt)\rangle|$. The M-dimensional subspace at time $t + dt$ is constructed by selecting adiabatic states with highest overlaps. The subspaces are then re-indexed in ascending order of energy and the corresponding physical quantity values are updated from the values in full space.

6. To carry out stochastic hopping between the PESs, we employ the crossing-classified and corrected algorithm.[47,48] We calculate the hopping probabilities g_i from the active state "a" to all other adiabatic states "i" in the subspace at time t within the conventional FSSH approach,[49]

$$g_i = \frac{2dt\,\text{Re}\left[w_a^*(t)w_i(t)\sum_k\left(v_k \cdot d_{ai}^{k,x} + \omega_k \cdot d_{ai}^{k,\theta}\right)\right]}{|w_a(t)|^2}. \quad (10)$$

Next, overlap between the active state "a" at time t and each adiabatic state in the subspace at time $t + dt$ is calculated and the state with maximum overlap "j" is selected. If $j \neq a$, the active state has encountered a crossing within the time interval and the corresponding hopping probability for state "j" is self-consistently corrected, $g_j = [|w_a(t)|^2 - |w_a(t+dt)|^2]/|w_a(t)|^2 - \sum_{i\neq j}g_i$.[53] If any of the calculated hopping probabilities is negative, it is reset to zero. A uniform random number $\zeta \in [0,1]$ is generated, and if $\sum_{i=1}^{b-1} g_i < \zeta \leq \sum_{i=1}^{b} g_i$, hopping to state "$b$" is assigned. If $b = j$, the new active state index becomes "j" without

even considering energy conservation. If $b \neq j$, the adiabatic state "k" in the subspace at time $t + dt$ is identified, which has maximum overlap with state "b" at time t. If the nuclear velocities can be readjusted, the new active state index is assigned to "k"; otherwise, it represents a frustrated hop, and the system remains on the "jth" adiabatic PES. The adjusted nuclear velocities from the active state "a" to the adiabatic state $b \neq j$ are given by

$$v'_k = v_k + d^{k,x}_{ab} \frac{A}{B} \left[\sqrt{1 + \frac{2(E_a - E_b)B}{A^2}} - 1 \right], \quad (11)$$

$$\omega'_k = \omega_k + d^{k,\theta}_{ab} \frac{A}{B} \left[\sqrt{1 + \frac{2(E_a - E_b)B}{A^2}} - 1 \right], \quad (12)$$

where

$$A = \sum_k \left(v_k d^{k,x}_{ab} + \omega_k d^{k,\theta}_{ab} \right)$$

and

$$B = \sum_k \left[\left(d^{k,x}_{ab} \right)^2 / m_k + \left(d^{k,\theta}_{ab} \right)^2 / I_k \right].$$

7. The energy-based decoherence correction of the wavefunction coefficients is carried out following the algorithm proposed by Zhu and co-workers[54] and further simplified by Granucci and Persico.[55] At each time step t, the decoherence time for an adiabatic state i (excluding the active state, $i \neq a$) is calculated by

$$\tau_i = \frac{\hbar \left(1 + \frac{C}{E_{kin}} \right)}{|E_i - E_a|}, \quad (13)$$

where C is a pre-fixed parameter ($C = 0.1$ hartree) and E_{kin} is the total nuclear kinetic energy. The wavefunction coefficients are then readjusted as

$$w'_i = \begin{cases} w_i \exp\left(-\frac{dt}{\tau_i} \right), & i \neq a, \\ \dfrac{w_i \left(1 - \sum_{k \neq a} |w'_k|^2 \right)^{1/2}}{|w_i|}, & i = a. \end{cases} \quad (14)$$

$|\Psi(t)\rangle$ is then expressed within the diabatic basis of monomer HOMOs $|k\rangle$ ($|\psi_i(t)\rangle = \sum_k c_{k,i}(t)|k\rangle$) and stored for post-calculation analysis.

8. Steps 2–7 are repeated until the wavepacket propagation is performed up to a predefined simulation time.

Steps 1–8 are repeated for a prefixed number of trajectories to simulate the non-adiabatic dynamics of the intra-chain charge-carrier transport.

The time-dependent mean-squared displacement (MSD) and inverse participation ratio (IPR) are calculated from the time-evolved wavefunction by[50]

$$MSD(t) = \frac{1}{N_{traj}} \sum_{i=1}^{N_{traj}} \left\langle \psi_a^{(i)}(t) | (r - r_0)^2 | \psi_a^{(i)}(t) \right\rangle, \quad (15)$$

$$IPR(t) = \frac{1}{N_{traj}} \sum_{i=1}^{N_{traj}} \frac{1}{\sum_k \left| \left\langle k | \psi_a^{(i)}(t) \right\rangle \right|^4}, \quad (16)$$

where $\psi_a^{(i)}(t)$ is the active state at time t along the ith trajectory and N_{traj} is the number of independent surface hopping trajectories. The matrix elements in Eqs. (15) and (16) are computed within the monomer-based diabatic basis, $\langle k|r^2|l \rangle = \delta_{kl} k^2 L^2$ and $\langle k|r|l \rangle = \delta_{kl} kL$, with L being the distance between the nearest-neighbor monomer components. Since the charge is initially placed at the central monomer of the chain, the reference position of the charge is $r_0 = NL/2$. To obtain a smooth profile of $MSD(t)$, we consider the following FSSH parameters—$N_{traj} = 10\,000$, $dt = 0.1$ fs, and $M = 10$.

III. RESULTS AND DISCUSSION

We have first parameterized the model against density functional theory (DFT) calculations on the reference polymer IDTBT (Fig. 1). We have calculated the HOMO energy levels for different IDTBT oligomers at the B3LYP/cc-pVDZ level using the Gaussian-16 package[56] and found that the energy of the HOMO level saturates for oligomers with more than four IDTBT units [Fig. 2(a)]. We have considered the IDTBT hexamer for further parameterization calculations and determined the electronic structure for varying torsion angles between the IDT and BT units. To reproduce the corresponding HOMO energy of the IDTBT hexamer at each torsional angle $\theta_{IDT,BT}$ within the tight-binding (TB) approach, both for the syn- and anti-conformations, we consider the HOMO energy of the isolated IDT (BT) moiety as the respective site energy $\varepsilon_{IDT(BT)} = -5.2(-6.7)$ eV and calculate the electronic coupling element $\beta|\cos(\theta_{IDT,BT})|$. A simple fitting of the electronic coupling elements as a function of $\theta_{IDT,BT}$ gives $|\beta| \sim 0.5$ eV [Fig. 2(b)]. The large value of β is expected for wide-band one-dimensional conjugated polymers, as reported in earlier study.[33]

To parameterize $\alpha_{IDT(BT)}$ driving charge localization, the neutral IDTBT hexamer as well as the corresponding cation have been optimized at the wB97XD/CC-PVDZ level of theory.[56] The hole density variation between the cation state (CA) and the neutral state (GS) is computed using Multiwfn program package.[57] Variation in charge density $\Delta\rho(r) = \rho_{CA}(r) - \rho_{GS}(r)$ is computed for each IDT (BT) unit within the neutral and cationic IDTBT oligomers (see Fig. 3). We have also repeated the calculations using the more
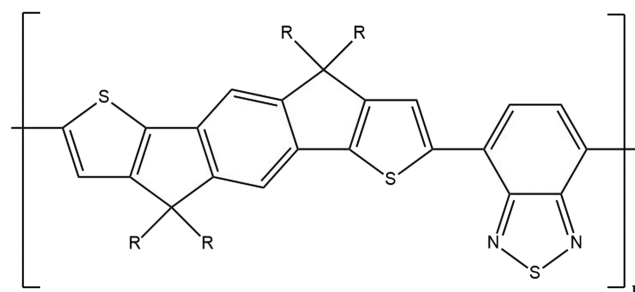

FIG. 1. Chemical structure of the indacenodithiophene-co-benzothiadiazole (IDTBT) polymer.
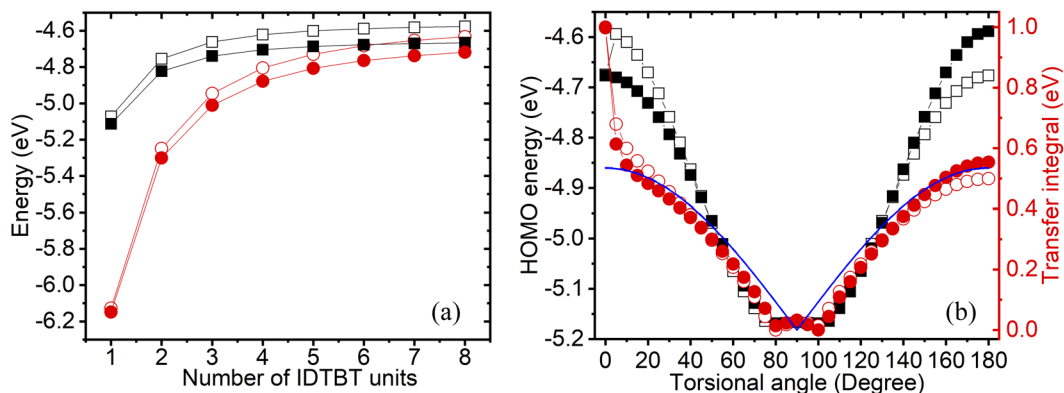
FIG. 2. (a) HOMO (black square) and HOMO-1 (red circle) energy levels of IDTBT oligomers, as calculated at the B3LYP/cc-pVDZ level. Filled (open) symbols represent anti-(syn-)conformation of the IDTBT chain. (b) HOMO energy levels of the IDTBT hexamer (black square) and nearest-neighbor transfer integrals (red circle) between IDT and BT units as a function of torsion angle. Filled (open) symbols represent the corresponding parameters for anti-(syn-)conformation of IDTBT. The blue solid (broken) line represents the fit of the transfer integrals with a cosine function for anti-(syn-)conformation, which almost overlap with each other. The fitting functions of the transfer integrals for anti- and syn-conformations are $0.379(1 + \cos 2\theta_{k,k-1})^{\frac{1}{2}}$ and $0.378(1 + \cos 2\theta_{k,k-1})^{\frac{1}{2}}$, respectively.

accurate long-range separated LC-wPBE functional but obtained similar charge localization profiles. Within the TB Hamiltonian, the DFT charge density profile for the fully optimized IDTBT chain carrying a positive charge is reproduced qualitatively considering $\alpha_{IDT(BT)}$ = 6100(6130) cm^{-1} Å^{-1} (Fig. 3).

The torsional potential profiles of several solid phases of IDTBT with different degrees of short- and long-range crystalline order have earlier been determined employing molecular mechanics/molecular dynamics simulations.[30] We fit the reported torsional potential of the non-interdigitated phase of IDTBT within a simple harmonic oscillator approximation and determine that the double-well
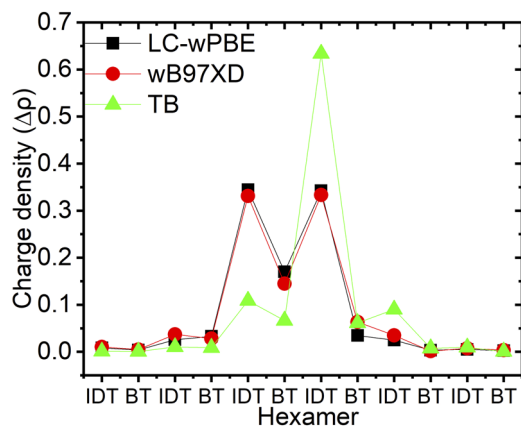

FIG. 3. Optimized charge density profile obtained within DFT employing the wB97XD functional (red circle) and LC-wPBE functional (black square). The optimized charge density distribution is confined over ~2–3 IDTBT units and well captured by the TB Hamiltonian (green triangle). TB modeling is done considering a polymer chain with an odd number of monomers (301 units) and an IDT moiety as the central unit where the charge is initially located, hence the asymmetric charge density profile.

potential is centered around $\theta_{eq} \sim 23°$ and $\theta'_{eq} \sim 153°$ with torsional stiffness constants K_θ = 2530 cm^{-1} and K'_θ = 5000 cm^{-1}, respectively. The other parameters are either taken from previous charge transport simulations in molecular crystals or conjugated polymers[21,33,43,47] (K_x = 14 500 amu ps^{-2} and γ = 100 ps^{-1}) or adjusted for IDT (BT) units [m_k = 265(135) amu and I_k = 178(221) amu Å^2].

Simulated $MSD(t)$ of the charge-carrier wavepackets at different T display linear evolution with time [Fig. 4(a)]. The linear time-evolution of $MSD(t)$ indicates that an equilibrium diffusion regime is attained, and the mobility values are computed from the equilibrium diffusion coefficients $(D = \frac{1}{2} \lim_{t \to \infty} d(MSD(t))/dt)$ using the Einstein relationship $(\mu = eD/k_BT)$.[21] The calculated $\mu(T)$ values well reproduce the T-dependence of experimentally measured hole-mobilities within IDTBT samples[58] [Fig. 5(a)] and also exhibits somewhat similar T-dependence to that reported for P3HT at moderate torsional stiffness.[33] Yet, the time-evolved IPR values (proxy of the charge-carrier delocalization length) are much smaller as compared to poly (3-hexylthiophene) (P3HT) [Fig. 4(b)], indicating the more localized nature of the charge carriers in the copolymer. $IPR(t)$ at low T also indicates that the available thermal energy is used to delocalize the wavepacket further before attaining the saturation value [Fig. 4(b)]. The total charge fraction over IDT and BT units at different time instants along the simulation path also indicates that the localized nature of the wavepacket gets retained even during the time propagation [Fig. 5(b)]. The time-dependent intra-chain charge-density profiles are shown in Fig. 6, which in sync with the total charge fraction over IDT and BT units [Fig. 5(b)] hints toward a superexchange-type mechanism recently proposed for donor–acceptor cocrystals and copolymers.[59–61] Within this mechanism, the HOMO orbitals of the acceptor units function as bridges between the HOMO orbitals of the donor moieties for hole transport, and the effective coupling between the neighboring donor units is mediated by the bridging acceptor via superexchange.[61] Consequently, the hole carriers are expected to remain localized
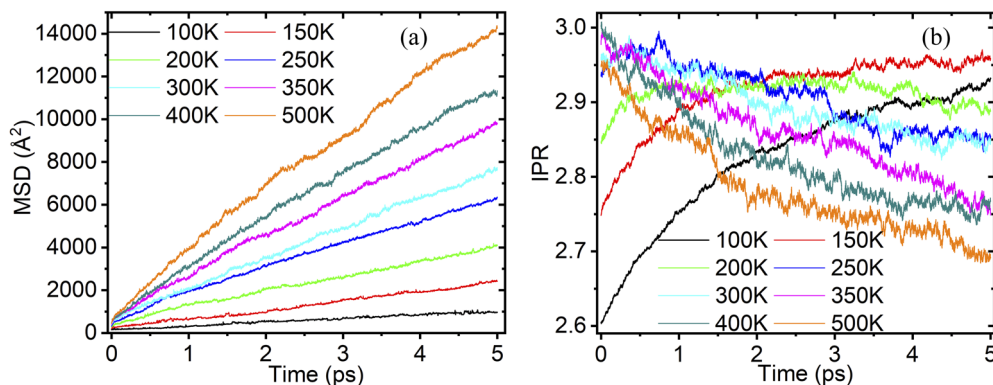
FIG. 4. Time evolution of (a) *MSD* and (b) *IPR* at various *T* for the IDTBT polymer chain with twisted equilibrium configuration. Color codes for varying *T* are indicated in the figure.

primarily on the donor units, e.g., on IDT units in the present study.

On repeating the calculations with similar torsional stiffness but varying equilibrium torsion angles (θ_{eq} and θ'_{eq}), we observe that D as well as the RT charge-carrier mobility decreases for more twisted IDTBT chains [Fig. 7(a)]. As has been predicted in an earlier study,[33] the amount of delocalization of the charge carrier in twisted chains results from the interplay between the classical forces felt by the ions and the electronic forces. The electronic forces favor a planar geometry and prompt higher charge delocalization, while the classical forces tend to confine the system closer to the equilibrium (twisted) ground-state geometry. This interplay explains the thermally activated behavior in Fig. 5(a), as the feedback effects from the electrons on the nuclei drive the polymer chains toward a more planar, higher-energy conformation, and is also supported by the RT-*IPR* profiles [Fig. 7(b)], which display reduced delocalization for twisted equilibrium geometries and remain on par with μ.

If we instead force the equilibrium geometry of the chains to be planar, an unexpected *T*-dependence of the charge-carrier mobility is obtained, with $\mu(T)$ showing *T*-activated behavior at low *T* but a power-law behavior at high *T* [Fig. 8(a)]. In homopolymers (e.g., P3HT) with planar equilibrium geometry, $\mu(T)$ shows a band-like transport over the entire temperature range with $\mu(T)$ decreasing with increasing *T* due to scattering with thermal phonons.[33] The average charge delocalization lengths within the copolymers [Fig. 8(b)] are also much smaller compared to that reported for the homopolymers in planar equilibrium geometry (*IPR* ~ 20).[33]

This unexpected *T*-dependence of charge-carrier mobility for planar equilibrium configuration as well as the lower values of mean *IPR* arises due to the *mismatch in on-site energy* (ε_k) between the donor and acceptor moieties. The IDTBT copolymer chains studied here can be viewed as multiple quantum wells, which explains why the charge carriers are less delocalized in space than in a homopolymer. To probe this effect, we have calculated the RT mobility in twisted copolymer chains as a function of the energy offset between
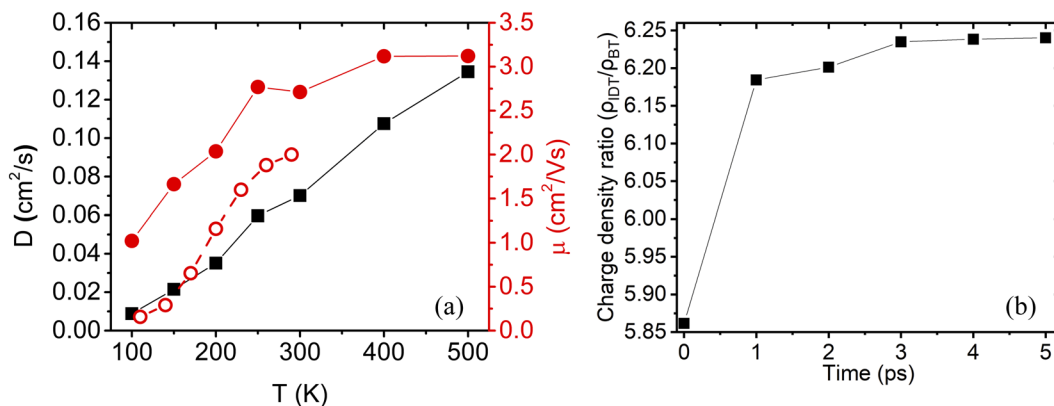

FIG. 5. (a) *T*-dependence of *D* (black filled square) and μ (red filled circle) within the IDTBT chain are shown. Experimentally measured hole-mobility values within the IDTBT sample at $V_g = -70$ V are reproduced from Ref. 58 and shown as open red circles with dashed lines. (b) Average ratio of the total charge densities over IDT and BT moieties at different stages of the 300 K simulation trajectories.
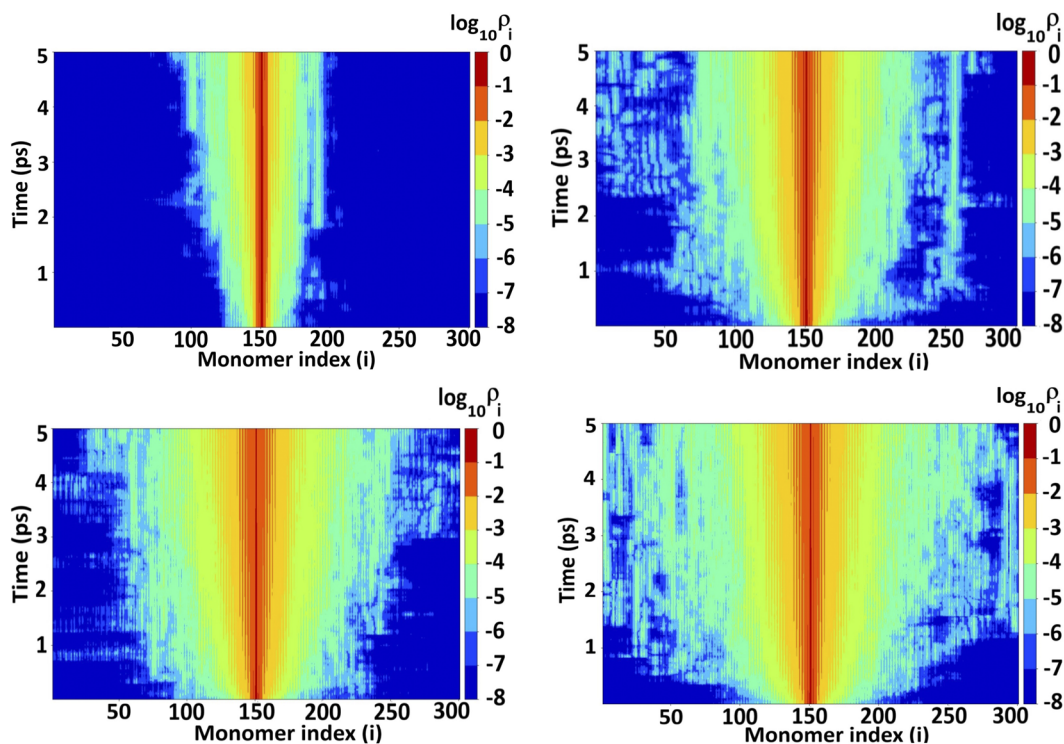
FIG. 6. Time-evolved charge density profile at T = 100 K (upper left), 200 K (upper right), 300 K (lower left), and 400 K (lower right). The color scale indicates the log of the normalized charge density.

the HOMO energies of the donor and acceptor moieties ($|\varepsilon_D - \varepsilon_A|$). As expected, μ decreases sharply with an increase in the energy mismatch [Fig. 9(a)]. The mean IPR values for different systems are consistent with the calculated μ values and represent more localized charge carriers in copolymers with a larger energy mismatch

[Fig. 9(b)]. This finding is similar to the results reported by Manurung and co-workers[32] for the inter-chain charge-carrier transport in copolymers, and consequently, copolymers with reduced energy difference between the composing monomer units should be targeted to realize high-mobility polymer semiconductors.
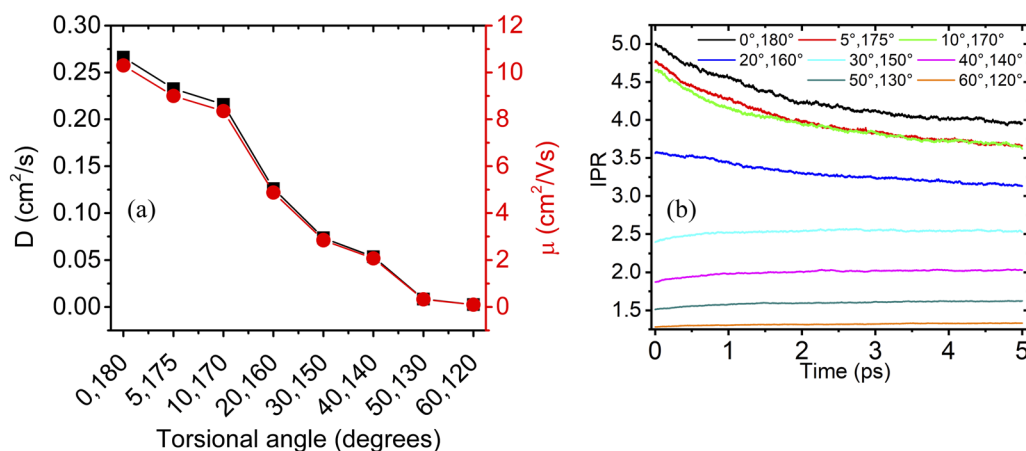

FIG. 7. Dependence of (a) D (black filled square) and RT mobility (red filled circle) on the equilibrium torsion angle θ_{eq}. (b) Corresponding $IPR(t)$ profiles as a function of θ_{eq} are shown. Color codes for varying θ_{eq} are indicated in the figure.

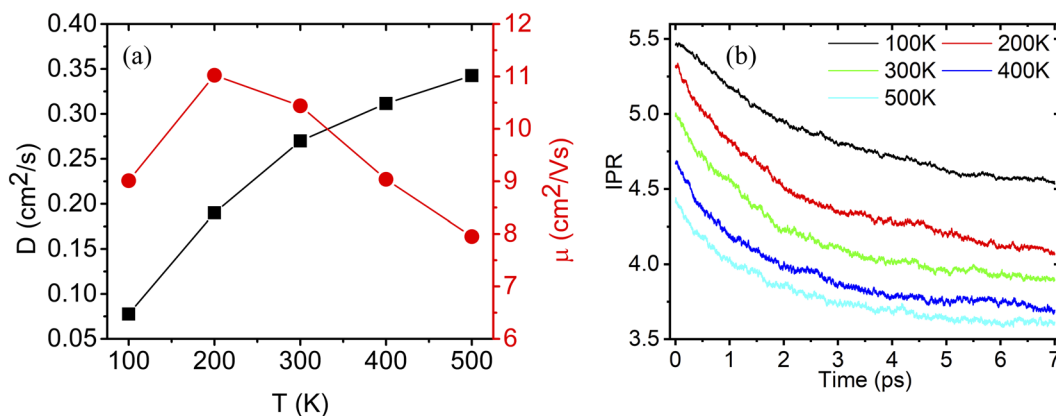**FIG. 8.** (a) *T*-dependence of *D* (black filled square) and *μ* (red filled circle) within the IDTBT chain for planar equilibrium geometry. (b) Corresponding *IPR*(*t*) profiles are shown. Color codes for varying *T* are indicated in the figure.
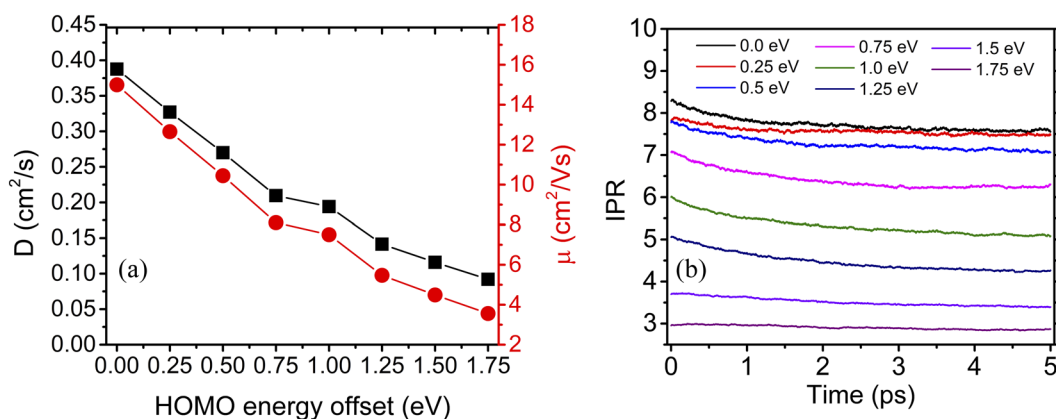

FIG. 9. (a) Dependence of D (black filled square) and intra-chain RT mobility (red filled circle) in copolymers with varying offsets in HOMO energies of the donor and acceptor moieties. (b) Corresponding *IPR*(*t*) profiles as a function of $|\varepsilon_D - \varepsilon_A|$ are shown. Color codes for varying $|\varepsilon_D - \varepsilon_A|$ are indicated in the figure.

IV. CONCLUSION

In conclusion, employing a mixed quantum–classical dynamics technique, we have studied the charge-carrier transport along conjugated copolymer chains and explored the effects of the polymer backbone structure and on-site energy mismatch on the charge-carrier mobility. Effective parameters employed in the simplified TB Hamiltonian were obtained from accurate quantum-chemical calculations. While the effects of the structure of the copolymer backbone on charge transport are similar to that in homopolymers, our study reveals that the energy mismatch between the component units can localize the charge carrier significantly and that a smaller frontier MO energy difference between the donor and acceptor moieties should result in higher charge-carrier mobility copolymers. We also reproduced the experimentally observed thermally activated *T*-dependence of the hole mobility in IDTBT, which arises because of the slightly out-of-plane equilibrium geometry of the polymer chains. We believe that the current model, in conjunction with first-principle calculations, can be extended to more complex copolymer structures in search for high-mobility polymeric materials. Yet, there is a need to extend the current formalism in order to account for relatively rare but important interchain contacts, as these provide the crossing points needed for charge percolation at the macroscopic scale. We close by noting that while the current on-chain transport model reproduces surprisingly well the temperature-dependent charge-carrier mobility, it slightly overshoots the mobility values, which are likely limited by the contact resistance at the crossing regions in these amorphous polymers.

AUTHOR DECLARATIONS

Conflict of Interest

The authors have no conflicts of interest to disclose.

Author Contributions

R.D. and S.P. contributed equally to this work.

DATA AVAILABILITY

The data that support the findings of this study are available from the corresponding author upon reasonable request.

REFERENCES

[1] A. C. Arias, J. D. MacKenzie, I. McCulloch, J. Rivnay, and A. Salleo, Chem. Rev. 110, 3 (2010).

[2] H. Sirringhaus, Adv. Mater. 26, 1319 (2014).

[3] J. Zaumseil and H. Sirringhaus, Chem. Rev. 107, 1296 (2007).

[4] J. H. Burroughes, D. D. C. Bradley, A. R. Brown, R. N. Marks, K. Mackay, R. H. Friend, P. L. Burns, and A. B. Holmes, Nature 347, 539 (1990).

[5] H. Sirringhaus, N. Tessler, and R. H. Friend, Science 280, 1741 (1998).

[6] A. Salleo, T. W. Chen, A. R. Völkel, Y. Wu, P. Liu, B. S. Ong, and R. A. Street, Phys. Rev. B 70, 115311 (2004).

[7] I. McCulloch, M. Heeney, C. Bailey, K. Genevicius, I. MacDonald, M. Shkunov, D. Sparrowe, S. Tierney, R. Wagner, W. Zhang, M. L. Chabinyc, R. J. Kline, M. D. McGehee, and M. F. Toney, Nat. Mater. 5, 328 (2006).

[8] D. Venkateshvaran, M. Nikolka, A. Sadhanala, V. Lemaur, M. Zelazny, M. Kepa, M. Hurhangee, A. J. Kronemeijer, V. Pecunia, I. Nasrallah, I. Romanov, K. Broch, I. McCulloch, D. Emin, Y. Olivier, J. Cornil, D. Beljonne, and H. Sirringhaus, Nature 515, 384 (2014).

[9] K. Kang, S. Watanabe, K. Broch, A. Sepe, A. Brown, I. Nasrallah, M. Nikolka, Z. Fei, M. Heeney, D. Matsumoto, K. Marumoto, H. Tanaka, S. Kuroda, and H. Sirringhaus, Nat. Mater. 15, 896 (2016).

[10] M. Xiao, R. L. Carey, H. Chen, X. Jiao, V. Lemaur, S. Schott, M. Nikolka, C. Jellett, A. Sadhanala, S. Rogers, S. P. Senanayak, A. Onwubiko, S. Han, Z. Zhang, M. Abdi-Jalebi, Y. Zhang, T. H. Thomas, N. Mahmoudi, L. Lai, E. Selezneva, X. Ren, M. Nguyen, Q. Wang, I. Jacobs, W. Yue, C. R. McNeill, G. Liu, D. Beljonne, I. McCulloch, and H. Sirringhaus, Sci. Adv. 7, eabe5280 (2021).

[11] M. Kim, S. U. Ryu, S. A. Park, K. Choi, T. Kim, D. Chung, and T. Park, Adv. Funct. Mater. 30, 1904545 (2020).

[12] V. Coropceanu, J. Cornil, D. A. da Silva Filho, Y. Olivier, R. Silbey, and J.-L. Brédas, Chem. Rev. 107, 926 (2007).

[13] T. Nematiaram and A. Troisi, J. Chem. Phys. 152, 190902 (2020).

[14] H. Bässler, Phys. Status Solidi 175, 15 (1993).

[15] J. Cornil, D. Beljonne, J.-P. Calbert, and J.-L. Brédas, Adv. Mater. 13, 1053 (2001).

[16] S. Athanasopoulos, J. Kirkpatrick, D. Martínez, J. M. Frost, C. M. Foden, A. B. Walker, and J. Nelson, Nano Lett. 7, 1785 (2007).

[17] A. Troisi and G. Orlandi, Phys. Rev. Lett. 96, 086601 (2006).

[18] S. Fratini and S. Ciuchi, Phys. Rev. Lett. 103, 266601 (2009).

[19] S. Fratini, S. Ciuchi, D. Mayou, G. T. de Laissardière, and A. Troisi, Nat. Mater. 16, 998 (2017).

[20] R. P. Fornari, P. W. M. Blom, and A. Troisi, Phys. Rev. Lett. 118, 086601 (2017).

[21] L. Wang and D. Beljonne, J. Phys. Chem. Lett. 4, 1888 (2013).

[22] L. Wang, O. V. Prezhdo, and D. Beljonne, Phys. Chem. Chem. Phys. 17, 12395 (2015).

[23] S. Giannini, A. Carof, M. Ellis, H. Yang, O. G. Ziogos, S. Ghosh, and J. Blumberger, Nat. Commun. 10, 3843 (2019).

[24] R. Noriega, A. Salleo, and A. J. Spakowitz, Proc. Natl. Acad. Sci. U. S. A. 110, 16315 (2013).

[25] S. Wang, S. Fabiano, S. Himmelberger, S. Puzinas, X. Crispin, A. Salleo, and M. Berggren, Proc. Natl. Acad. Sci. U. S. A. 112, 10599 (2015).

[26] X. Zhang, H. Bronstein, A. J. Kronemeijer, J. Smith, Y. Kim, R. J. Kline, L. J. Richter, T. D. Anthopoulos, H. Sirringhaus, K. Song, M. Heeney, W. Zhang, I. McCulloch, and D. M. DeLongchamp, Nat. Commun. 4, 2238 (2013).

[27] Y. Tsutsui, G. Schweicher, B. Chattopadhyay, T. Sakurai, J.-B. Arlin, C. Ruzié, A. Aliev, A. Ciesielski, S. Colella, A. R. Kennedy, V. Lemaur, Y. Olivier, R. Hadji, L. Sanguinet, F. Castet, S. Osella, D. Dudenko, D. Beljonne, J. Cornil, P. Samorì, S. Seki, and Y. H. Geerts, Adv. Mater. 28, 7106 (2016).

[28] T. H. Thomas, D. J. Harkin, A. J. Gillett, V. Lemaur, M. Nikolka, A. Sadhanala, J. M. Richter, J. Armitage, H. Chen, I. McCulloch, S. M. Menke, Y. Olivier, D. Beljonne, and H. Sirringhaus, Nat. Commun. 10, 2614 (2019).

[29] R. Noriega, Macromol. Rapid Commun. 39, 1800096 (2018).

[30] V. Lemaur, J. Cornil, R. Lazzaroni, H. Sirringhaus, D. Beljonne, and Y. Olivier, Chem. Mater. 31, 6889 (2019).

[31] M. Reisjalali, J. J. Burgos-Mármol, R. Manurung, and A. Troisi, Phys. Chem. Chem. Phys. 23, 19693 (2021).

[32] R. Manurung, P. Li, and A. Troisi, J. Phys. Chem. B 125, 6338 (2021).

[33] S. Prodhan, J. Qiu, M. Ricci, O. M. Roscioni, L. Wang, and D. Beljonne, J. Phys. Chem. Lett. 11, 6519 (2020).

[34] F. C. Grozema and L. D. A. Siebbeles, J. Phys. Chem. Lett. 2, 2951 (2011).

[35] A. R. Cook, S. Asaoka, X. Li, and J. R. Miller, J. Phys. Chem. Lett. 10, 171 (2019).

[36] A. J. Sneyd, T. Fukui, D. Paleček, S. Prodhan, I. Wagner, Y. Zhang, J. Sung, S. M. Collins, T. J. A. Slater, Z. Andaji-Garmaroudi, L. R. MacFarlane, J. D. Garcia-Hernandez, L. Wang, G. R. Whittell, J. M. Hodgkiss, K. Chen, D. Beljonne, I. Manners, R. H. Friend, and A. Rao, Sci. Adv. 7, eabh4232 (2021).

[37] R. Binder, D. Lauvergnat, and I. Burghardt, Phys. Rev. Lett. 120, 227401 (2018).

[38] R. Binder and I. Burghardt, J. Chem. Phys. 152, 204120 (2020).

[39] J. Spencer, F. Gajdos, and J. Blumberger, J. Chem. Phys. 145, 064102 (2016).

[40] S. Giannini, A. Carof, and J. Blumberger, J. Phys. Chem. Lett. 9, 3116 (2018).

[41] S. Prodhan, S. Giannini, L. Wang, and D. Beljonne, J. Phys. Chem. Lett. 12, 8188 (2021).

[42] L. Wang, A. V. Akimov, L. Chen, and O. V. Prezhdo, J. Chem. Phys. 139, 174109 (2013).

[43] X. Bai, J. Qiu, and L. Wang, J. Chem. Phys. 148, 104106 (2018).

[44] R. P. Fornari and A. Troisi, Adv. Mater. 26, 7627 (2014).

[45] R. P. Fornari, J. Aragó, and A. Troisi, J. Chem. Phys. 142, 184105 (2015).

[46] W. P. Su, J. R. Schrieffer, and A. J. Heeger, Phys. Rev. Lett. 42, 1698 (1979).

[47] J. Qiu, X. Bai, and L. Wang, J. Phys. Chem. Lett. 9, 4319 (2018).

[48] J. Qiu, X. Bai, and L. Wang, J. Phys. Chem. Lett. 10, 637 (2019).

[49] J. C. Tully, J. Chem. Phys. 93, 1061 (1990).

[50] L. Wang, J. Qiu, X. Bai, and J. Xu, Wiley Interdiscip. Rev.: Comput. Mol. Sci. 10, e1435 (2020).

[51] G. Granucci, M. Persico, and A. Toniolo, J. Chem. Phys. 114, 10608 (2001).

[52] F. Plasser, G. Granucci, J. Pittner, M. Barbatti, M. Persico, and H. Lischka, J. Chem. Phys. 137, 22A514 (2012).

[53] L. Wang and O. V. Prezhdo, J. Phys. Chem. Lett. 5, 713 (2014).

[54] C. Zhu, S. Nangia, A. W. Jasper, and D. G. Truhlar, J. Chem. Phys. 121, 7658 (2004).

[55] G. Granucci and M. Persico, J. Chem. Phys. 126, 134114 (2007).

[56] M. J. Frisch, G. W. Trucks, H. B. Schlegel, G. E. Scuseria, M. A. Robb, J. R. Cheeseman, G. Scalmani, V. Barone, G. A. Petersson, H. Nakatsuji, X. Li, M. Caricato, A. V. Marenich, J. Bloino, B. G. Janesko, R. Gomperts, B. Mennucci, H. P. Hratchian, J. V. Ortiz, A. F. Izmaylov, J. L. Sonnenberg, D. Williams-Young, F. Ding, F. Lipparini, F. Egidi, J. Goings, B. Peng, A. Petrone, T. Henderson, D. Ranasinghe, V. G. Zakrzewski, J. Gao, N. Rega, G. Zheng, W. Liang, M. Hada,

M. Ehara, K. Toyota, R. Fukuda, J. Hasegawa, M. Ishida, T. Nakajima, Y. Honda, O. Kitao, H. Nakai, T. Vreven, K. Throssell, J. A. Montgomery, Jr., J. E. Peralta, F. Ogliaro, M. J. Bearpark, J. J. Heyd, E. N. Brothers, K. N. Kudin, V. N. Staroverov, T. A. Keith, R. Kobayashi, J. Normand, K. Raghavachari, A. P. Rendell, J. C. Burant, S. S. Iyengar, J. Tomasi, M. Cossi, J. M. Millam, M. Klene, C. Adamo, R. Cammi, J. W. Ochterski, R. L. Martin, K. Morokuma, O. Farkas, J. B. Foresman, and D. J. Fox, GAUSSIAN 16, Revision C.01, Gaussian, Inc., Wallingford, CT, 2016.

[57] T. Lu and F. Chen, J. Comput. Chem. **33**, 580 (2012).

[58] S. Schott, U. Chopra, V. Lemaur, A. Melnyk, Y. Olivier, R. Di Pietro, I. Romanov, R. L. Carey, X. Jiao, C. Jellett, M. Little, A. Marks, C. R. McNeill, I. McCulloch, E. R. McNellis, D. Andrienko, D. Beljonne, J. Sinova, and H. Sirringhaus, Nat. Phys. **15**, 814 (2019).

[59] L. Zhu, Y. Yi, Y. Li, E.-G. Kim, V. Coropceanu, and J.-L. Brédas, J. Am. Chem. Soc. **134**, 2340 (2012).

[60] H. Geng, X. Zheng, Z. Shuai, L. Zhu, and Y. Yi, Adv. Mater. **27**, 1443 (2015).

[61] H. Geng, L. Zhu, Y. Yi, D. Zhu, and Z. Shuai, Chem. Mater. **31**, 6424 (2019).